Science Advances
AAAS

Supplementary Materials for

Perfect anomalous reflectors at optical frequencies

Tao He, Tong Liu, Shiyi Xiao, Zeyong Wei, Zhanshan Wang*, Lei Zhou*, Xinbin Cheng*

*Corresponding author. Email: wangzs@tongji.edu.cn (Z.Wa.); phzhou@fudan.edu.cn (L.Z.); chengxb@tongji.edu.cn (X.C.)

Published 2 March 2022, *Sci. Adv.* **8**, eabk3381 (2022)
DOI: 10.1126/sciadv.abk3381

This PDF file includes:

Supplementary Text

1. <u>The ideal energy-flow distribution of perfect anomalous reflection</u>

In a general situation, when a normal incident TM wave (E_i, H_i) impinges the metasurface, there are three channels $(E_r^{-1}, H_r^{-1}, E_r^0, H_r^0, E_r^{+1}, H_r^{+1})$ scattering the incident wave due to the periodicity as shown in Fig. S1A. Then, the electric and magnetic field of total field at $z = 0$ plane can be written as:

$$\begin{aligned} E_{total,x} &= E_i\left(1-r^0e^{j\varphi^0}-r^{-1}\cos\theta_r e^{-jGx+j\varphi^{-1}}-r^{+1}\cos\theta_r e^{+jGx+j\varphi^{+1}}\right) \\ H_{total,y} &= y_0E_i\left(1+r^0e^{j\varphi^0}+r^{-1}e^{-jGx+j\varphi^{-1}}+r^{+1}e^{+jGx+j\varphi^{+1}}\right) \end{aligned}, \tag{S1}$$

where $(r^{-1})^2cos\theta_r + (r^0)^2 + (r^{+1})^2cos\theta_r = 1$ satisfys energy conservation. G is the reciprocal lattice vector, and equals to $k_0 sin\theta_r$.

According to the electric and magnetic field, we can obtain the actual energy-flow distribution by $S_{pz} = \frac{1}{2}Re\left(E_{total,x}H^*_{total,y}\right)$. The actual energy-flow distribution can be written as:

$$S^a_{pz,z=0}(x) = \frac{1}{2}y_0E_i^2\left\{\mathrm{Re}\left[\begin{array}{c}\left(1-r^0e^{j\varphi^0}\right)r^{-1}e^{+jGx-j\varphi^{-1}}+\left(1-r^0e^{j\varphi^0}\right)r^{+1}e^{-jGx-j\varphi^{+1}} \\ -r^{-1}\cos\theta_r e^{-jGx+j\varphi^{-1}}\left(1+r^0e^{-j\varphi^0}\right) \\ -r^{+1}\cos\theta_r e^{+jGx+j\varphi^{+1}}\left(1+r^0e^{-j\varphi^0}\right) \\ -2r^{-1}r^{+1}\cos\theta_r\cos\left(2Gx-\varphi^{-1}+\varphi^{+1}\right)\end{array}\right]\right\}. \tag{S2}$$

The distribution of imperfect anomalous reflection Equation S2 is in form of

$$S^a(x) = A_1^a\cos\left(Gx+\tau_1^a\right)+A_2^a\cos\left(2Gx+\tau_2^a\right). \tag{S3}$$

The distribution is composed of first-order and second-order oscillations. The second-order oscillation comes from the interference between -1st and +1st channels, and the first-order oscillation is originated from the interference between the 0th and ±1st channels. When the -1st- and 0th-order light are suppressed well like Fig. S1B, that is perfect anomalous reflection, the r^0 and r^{-1} are zero. We can get the energy-flow distribution of perfect anomalous reflection. It can be obtained directly by Equation S2 that $S_{pz} = \frac{1}{2}y_0E_i^2r^{+1}cos(Gx+\varphi^{+1})(1-cos\theta_r)$. From energy conservation, the r^{+1} equals to $1/\sqrt{cos\theta_r}$. So the energy-flow distribution of perfect anomalous reflection is

$$S_{pz} = \frac{1}{2}y_0E_i^2\left(\frac{1}{\sqrt{\cos\theta_r}}-\sqrt{\cos\theta_r}\right)\cos\left(Gx+\varphi^{+1}\right), \tag{S4}$$

which is represented by

$$S(x) = A\cos\left(Gx+\tau\right). \tag{S5}$$

In order to realize perfect anomalous reflection, the metasurfaces need to minimize the second-order oscillation and modulate the first-order oscillation to match the required energy-flow distribution.

However, it's worth pointing out that Equation S4 is only a necessary condition for perfect anomalous reflection, but not a sufficient and necessary condition. In other words, the premise for the realization of perfect anomalous reflection is to make the energy-flow distribution meet

Equation S4, but energy-flow distribution in accordance with Equation S4 cannot necessarily achieves perfect anomalous reflection. For example, when $r^{-1} = 0$, the Equation S4 is simplified as

$$S^{a}_{pz,z=0}(x) = \frac{1}{2} y_0 E_i^2 \begin{bmatrix} r^{+1}(1-\cos\theta_r)\cos\left(Gx+\varphi^{+1}\right) \\ -r^{0}r^{+1}(1+\cos\theta_r)\cos\left(Gx+\varphi^{+1}-\varphi^{0}\right) \end{bmatrix}. \tag{S6}$$

For the convenience of derivation, let $\varphi_0 = 0$, and Equation S6 is further simplified as

$$S^{a}_{pz,z=0}(x) = \frac{1}{2} y_0 E_i^2 \cos\left(Gx+\varphi^{+1}\right) r^{+1}\left(1-\cos\theta_r - r^{0} - r^{0}\cos\theta_r\right). \tag{S7}$$

Let Equation S4 and Equation S7 equal, then

$$\left(\frac{1}{\sqrt{\cos\theta_r}} - \sqrt{\cos\theta_r}\right) = r^{+1}\left(1-\cos\theta_r - r^{0} - r^{0}\cos\theta_r\right). \tag{S8}$$

Substitute $(r^0)^2 + (r^{+1})^2\cos\theta_r = 1$ into Equation S8, then

$$\left[1-\left(r^{0}\right)^2\right]\left(1-\cos\theta_r - r^{0} - r^{0}\cos\theta_r\right)^2 = \left(1-\cos\theta_r\right)^2. \tag{S9}$$

Equation S9 is a quartic equation for the 0th-order reflection coefficient r^0. For any θ_r, the equation has a solution $r^0 = 0$, which is corresponding to perfect anomalous reflection. In addition, there are the other positive real solutions for the equation, which is corresponding to imperfect anomalous reflection. To sum up, the necessary condition to achieve perfect anomalous reflection is to make the energy-flow distribution meet Equation S4.

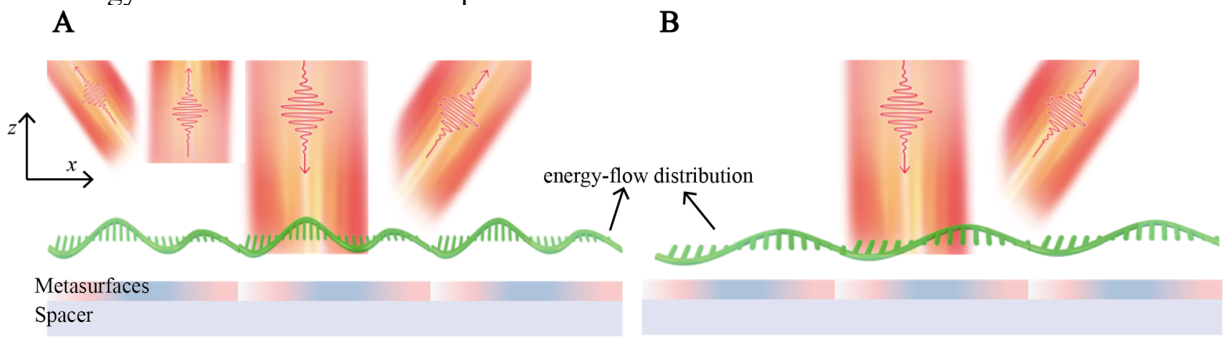

Fig. S1. The comparisons of imperfect and perfect anomalous reflection. (A) The energy-flow distribution of imperfect anomalous reflection is composed of first-order and second-order oscillations. **(B)** The energy-flow distribution of perfect anomalous reflection is composed of first-order oscillation.

2. ***The lateral energy transfer in structure***

A metasurface needs to modulate the energy-flow distribution in line with the simplified form to realize perfect anomalous reflection. Because the system has no active or lossy elements, we can get the relationship of energy-flow distribution around the metasurface:

$$\int_{x_0}^{x_0+dx}\left[S_{pz}\left(x,z=0\right)-S_{pz}\left(x,z=-z_0\right)\right]dx=\int_{-z_0}^{0}\left[S_{px}\left(x_0,z\right)-S_{px}\left(x_0+dx,z\right)\right]dz\,. \tag{S10}$$

According to the energy conservation, where S_{pz} and S_{px} are the z and x components of the Poynting vector. In a system without transmission loss, the S_{pz} in the bottom of metasurface ($z = -z_0$) is zero. Therefore, the relationship of energy-flow distribution is simplified as:

$$\int_{x_0}^{x_0+\Delta x}S_{pz}\left(x,z=0\right)dx=\int_{-z_0}^{0}\left[S_{px}\left(x_0,z\right)-S_{px}\left(x_0+\Delta x,z\right)\right]dz\,. \tag{S11}$$

The relationship tells us that it is an effective way utilizing lateral energy transfer S_{px} to modulate the actual energy-flow distribution S_{pz} precisely to realize the nonlocal requirements.

When impinges metasurfaces, the incident wave would be scattered into the spacer via propagating waves and also coupled into Bloch waves inside the top-layer metasurface. As shown in Fig. S2, the propagating waves are reflected by the bottom boundary. The high-order propagating waves are evanescent waves or weak enough to neglect. The electric fields of propagating waves are denoted by $c_{-1}^{\pm}$, $c_{0}^{\pm}$ and $c_{+1}^{\pm}$. The downward and upward propagating waves at the top of spacer are connected by the response of the bottom boundary and phase accumulation in spacer. That is $c_0^+ = c_0^- r_0 e^{j\Phi_0}$ and $c_{\pm1}^+ = c_{\pm1}^- r_1 e^{j\Phi_1}$, where $\Phi_0 = 2k_{0,z}^s h_s + \phi_0$ and $\Phi_1 = 2k_{\pm1,z}^s h_s + \phi_1$. The h_s is the thickness of spacer. Because h_s can't control Φ_0 and Φ_1 independently, we will mainly discuss the ability of phase responses ϕ_0 and ϕ_1. Then, the field distributions in spacer are given by:

$$\begin{aligned}
E_x &= \left[c_0^-\left(1-r_0e^{j\Phi_0}\right)+c_{-1}^-\left(1-r_1e^{j\Phi_1}\right)e^{-jGx}\cos\theta_1+c_{+1}^-\left(1-r_1e^{j\Phi_1}\right)e^{+jGx}\cos\theta_1\right]\\
E_z &= \left[-c_{-1}^-\left(1+r_1e^{j\Phi_1}\right)e^{-jGx}+c_{+1}^-\left(1+r_1e^{j\Phi_1}\right)e^{+jGx}\right]\sin\theta_1\\
H_y &= Y_0\left[c_0^-\left(1+r_0e^{j\Phi_0}\right)+c_{-1}^-\left(1+r_1e^{j\Phi_1}\right)e^{-jGx}+c_{+1}^-\left(1+r_1e^{j\Phi_1}\right)e^{+jGx}\right]
\end{aligned}\,. \tag{S12}$$

The lateral energy transfer at the top of spacer can be obtained by combining these formulas,

$$S_{px,z=-h}^{P}\left(x\right)=-\frac{1}{2}\mathrm{Re}\left(E_zH_y^*\right)=-\frac{1}{2}\sin\theta_1Y_0\,\mathrm{Re}\left[\sum_{i=1}^{6}\nu_i\right], \tag{S13}$$

where:

$$\begin{aligned}
\nu_1+\nu_4 &= \left(1+r_0e^{-j\Phi_0}\right)\left(1+r_1e^{j\Phi_1}\right)\left(-c_{-1}^-e^{-jGx}+c_{+1}^-e^{+jGx}\right)c_0^{-*}\\
\nu_2+\nu_6 &= \left|1+r_1e^{j\Phi_1}\right|^2\left(-\left|c_{-1}^-\right|^2+\left|c_{+1}^-\right|^2\right)\\
\nu_3+\nu_5 &= 2i\left|1+r_1e^{j\Phi_1}\right|^2\mathrm{Im}\left(c_{-1}^-c_{+1}^{-*}e^{-2jGx}\right)
\end{aligned}\,. \tag{S14}$$

$\nu_3 + \nu_5$ has no contribution to $S_{px,z=-h}^{P}(x)$. From what has been discussed above,

$$S_{px,z=-h}\left(x\right)=-\frac{1}{2}\sin\theta_1Y_0\,\mathrm{Re}\left[\begin{array}{c}\left(1+r_0e^{-j\Phi_0}\right)\left(1+r_1e^{j\Phi_1}\right)\left(-c_{-1}^-e^{-jGx}+c_{+1}^-e^{+jGx}\right)c_0^{-*}\\+\left|1+r_1e^{j\Phi_1}\right|^2\left(-\left|c_{-1}^-\right|^2+\left|c_{+1}^-\right|^2\right)\end{array}\right]. \tag{S15}$$

Similarly, the lateral energy transfer at other height in spacer can be obtained. The overall effect of lateral energy transfer in spacer can be given by:

$$S^P(x) = \int_{-z_0}^{-h} S^P_{px,z}(x)\,dz = S^P_{pz,z=-h}(x) - S^P_{pz,z=-z_0}(x). \tag{S16}$$

The $S^P_{pz,z=-z_0}$ is zero for no transmission in the system. Then, the $S^P_{pz,z=-h}$ can be obtained by:

$$S^P_{pz,z=-h}(x) = \frac{1}{2}\mathrm{Re}\left(E_x H_y^*\right) = \frac{1}{2} Y_0\,\mathrm{Re}\left[\sum_{i=1}^{9} s_i\right], \tag{S17}$$

where:

$$\begin{aligned}
s_1 + s_2 &= c_0^- \left(1 - r_0 e^{j\Phi_0}\right)\left(1 + r_1 e^{-j\Phi_1}\right)\left(c_{-1}^{-*} e^{+jGx} + c_{+1}^{-*} e^{-jGx}\right) \\
s_3 + s_4 &= c_0^{-*} \left(1 + r_0 e^{-j\Phi_0}\right)\left(1 - r_1 e^{j\Phi_1}\right)\left(c_{-1}^{-} e^{-jGx} + c_{+1}^{-} e^{+jGx}\right)\cos\theta_1 \\
s_5 + s_6 &= 2\cos\theta_1 \left(1 + r_1 e^{-j\Phi_1} - r_1 e^{j\Phi_1} - r_1^2\right)\mathrm{Re}\left(c_{+1}^{-} c_{-1}^{-*} e^{+j2Gx}\right) \\
s_7 &= \left|c_0^-\right|^2 \left(1 + r_0 e^{-j\Phi_0} - r_0 e^{j\Phi_0} - r_0^2\right) \\
s_8 &= \left|c_{-1}^-\right|^2 \left(1 + r_1 e^{-j\Phi_1} - r_1 e^{j\Phi_1} - r_1^2\right)\cos\theta_1 \\
s_9 &= \left|c_{+1}^-\right|^2 \left(1 + r_1 e^{-j\Phi_1} - r_1 e^{j\Phi_1} - r_1^2\right)\cos\theta_1
\end{aligned} \tag{S18}$$

When r_0 and r_1 are 1, the $s_5 + s_6$, s_7, s_8 and s_9 are imaginary number. Therefore, the lateral energy transfer in spacer can be simplified as

$$S^P(x) = \frac{1}{2} Y_0\,\mathrm{Re}\left[\begin{array}{c} c_0^- \left(1 - e^{j\Phi_0}\right)\left(1 + e^{-j\Phi_1}\right)\left(c_{-1}^{-*} e^{+jGx} + c_{+1}^{-*} e^{-jGx}\right) + \\ c_0^{-*} \left(1 + e^{-j\Phi_0}\right)\left(1 - e^{j\Phi_1}\right)\left(c_{-1}^{-} e^{-jGx} + c_{+1}^{-} e^{+jGx}\right)\cos\theta_1 \end{array}\right]. \tag{S19}$$

On the one hand, propagating waves in the spacer generate a cosine-form lateral energy transfer S^P when the amplitudes of propagating waves are 1. On the other hand, the phase responses ϕ_0 and ϕ_1 of the bottom boundary have a direct regulation on S^P.

In the metasurfaces region, the incident light is coupled into Bloch waves by the structure. As shown in reference (*42-44*), the field distributions in the metasurfaces are given by:

$$\begin{aligned}
E_x &= \sum_m S_m(z)\, e^{jGmx} \\
E_z &= \sum_m f_m(z)\, e^{jGmx} \\
H_y &= \sqrt{\frac{\varepsilon_0}{\mu_0}} \sum_m U_m(z)\, e^{jGmx}
\end{aligned} \tag{S20}$$

m is the order of Bloch waves. The $S_m(z)$, $f_m(z)$ and $U_m(z)$ include the downward and upward waves. The lateral energy transfer in the metasurfaces can be obtained as that in the spacer. However, the amplitudes of downward Bloch modes and upward Bloch modes are not same. Further, the amplitudes of high order Bloch modes are small. Then, the lateral energy transfer of Bloch waves is composed of first-order and second-order cosine functions because the high-order Bloch waves cancel each other. The results can also be understood in other respects that the actual energy-flow distribution S^a comes from the combined action of lateral energy transfers of propagating wave S^P and Bloch wave S^B, so the high-order Bloch waves cancel each other to produce the form of S^B. Besides, at the bottom of metasurfaces, according to boundary conditions,

the tangential components of electric and magnetic field are continuous. The field distribution in spacer can control the field in metasurfaces indirectly. In this way, the phase responses ϕ_0 and ϕ_1 of bottom boundary have an indirect influence on S^B.

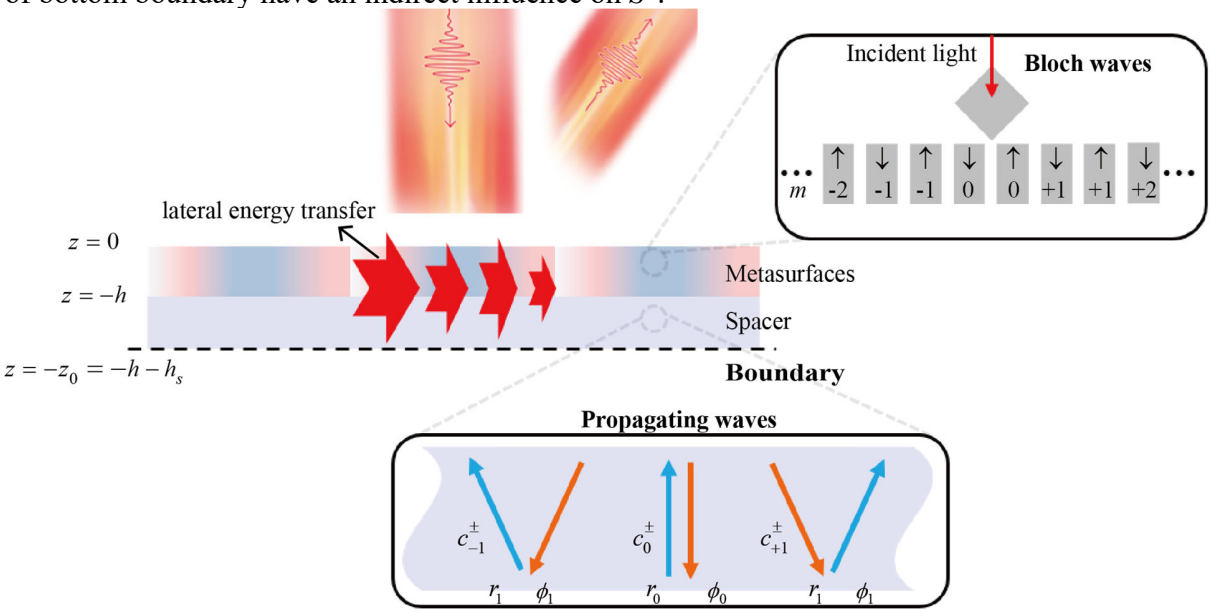

Fig. S2. Schematic diagram of Propagating waves and Bloch waves.

3. *The influence of phase response ϕ_0 and ϕ_1 on lateral energy transfer*

For the lateral energy transfer S^P, the amplitude A_1^P and phase shift τ_1^P determine the shape of function. As for the lateral energy transfer S^B, the amplitude and phase shift of each order together determine the form of lateral energy transfer. Fig. S3 shows how phase responses ϕ_0 and ϕ_1 affect the amplitudes and phase shifts of S^P and S^B. It can be seen that the amplitude A_1^P can be regulated in a large range and the phase shift τ_1^P is covering 0~2π, which indicates the strong ability of phase response ϕ_0 and ϕ_1 on lateral energy transfer S^P. Similarly, the amplitudes A_1^B, A_2^B and phase shifts τ_1^B, τ_2^B of lateral energy transfer S^B can also be regulated in a large range. The coefficients of lateral energy transfer S^P and S^B are calculated by a simplified model mentioned in the last section. It is not perfectly accurate but reflects the primary physical images.

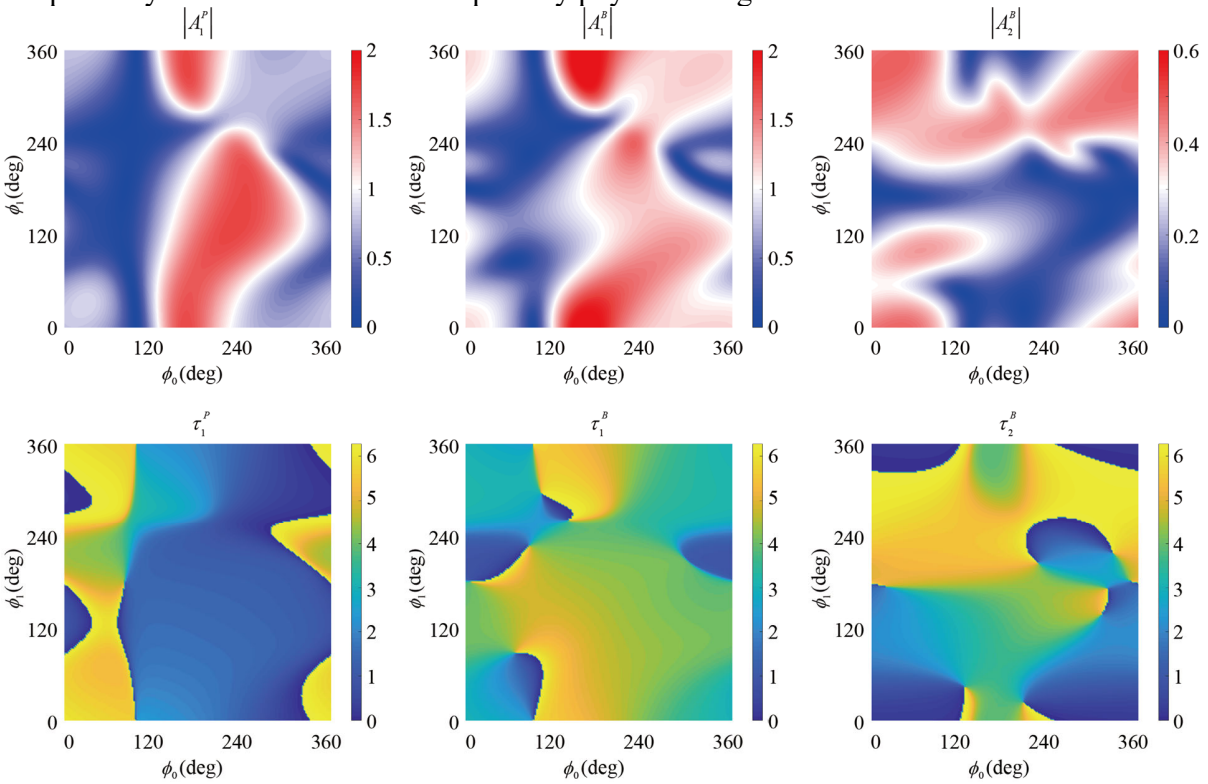

Fig. S3. The influence of ϕ_0 and ϕ_1 on parameters of lateral energy transfer.

4. The design process for multilayer

The multilayer films are designed to modulate the propagating waves according to the requirements from the perfect anomalous reflection. Therefore, the first step is to determine the condition of propagating waves. The multilayer is homogeneous in x direction, so only 0^{th}- and 1^{st}-order propagating waves need to be considered. In the case of 40º perfect anomalous reflection, the incident angles of 0^{th}- and 1^{st}-order propagating waves are 0º and 25.9º. The amplitude and phase response of 0^{th}-order propagating wave are 1 and 173º; amplitude and phase response of 1^{st}-order propagating wave are 1 and 170º. The multilayer has to satisfy the amplitude and phase response simultaneously. The traditional periodic Bragg mirror in Fig. S4A can offer near 100% reflectance only with proper proportion of high and low refractive index materials, as shown in Fig. S4B. In the region with high reflectance, the phase responses ϕ_0 and ϕ_1 are associated as the thickness changes, shown in main text. Generally speaking, periodic Bragg mirror with high reflectance is consisting of high- and low-refractive-index materials whose thicknesses are quarter wavelength optical thickness, that are $\lambda/4n_{high}$ and $\lambda/4n_{low}$. When the relationship between refractive index and thickness is broken, the reflectance would drop rapidly. By changing the refractive index (materials), the different Bragg mirror can be realized, but the phase combination of ϕ_0 and ϕ_1 is still associated under the condition of high reflectance. Hence, we use an aperiodic multilayer film as shown in Fig. 2G in the main text to realize arbitrary phase combination. We use a quarter-wave stack design high-reflection film to guarantee the amplitude requirement, and change the thicknesses of four outermost layers to guarantee the phase requirement. The aperiodic multilayer films are composed of a periodic Bragg mirror ($(HL)^7H$) and four phase layers (DCBA), where H is 109 nm and L is 263 nm. The Fig. S4C-F give the phase combination realized by aperiodic multilayer films with different phase layers. The phase control ability of the aperiodic multilayer films becomes stronger with the increase of phase layers. Hence, four phase layers are adopted to guarantee arbitrary phase combination of ϕ_0 and ϕ_1. Due to the good ability controlling the amplitude and phase of electromagnetic waves, there are a variety of multilayer satisfying the requirement. Fig. S4G-I shows the thickness of each layer and the spectra. As for 75º perfect anomalous reflection, the incident angles of 0^{th}- and 1^{st}-order propagating waves are 0º and 40.9º. The amplitude and phase response of 0^{th}-order propagating waves are 1 and 170º; amplitude and phase response of 1^{st}-order propagating waves are 1 and 149º. The multilayers satisfying the requirement are also listed in Fig. S4J-L.

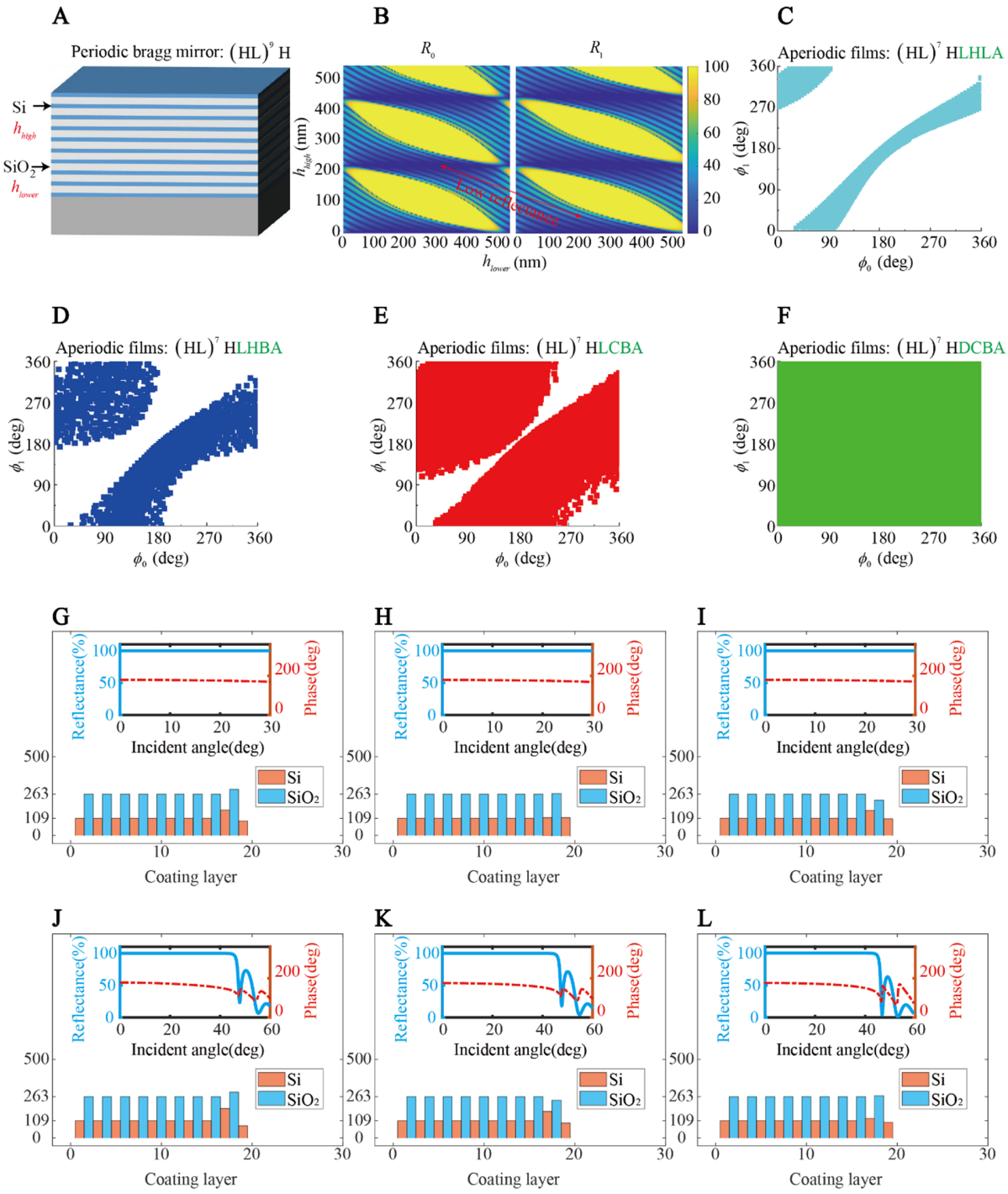

Fig. S4. The multilayer films satisfying the requirement of phase response. (A) The schematic diagram of periodic Bragg mirror. **(B)** The periodic Bragg mirror can offer near 100% reflectance only with proper proportion of high and low refractive index materials. In the region with high reflectance, the phase responses ϕ_0 and ϕ_1 are associated as the thickness changes, as shown in main text. In order to realize arbitrary phase combination, we propose to use aperiodic multilayer films as shown in Fig. 2G in the main text. **(C)-(F)** The phase combination realized by aperiodic

multilayer films with different phase layers. Four phase layers are adopted to guarantee arbitrary phase combination of ϕ_0 and ϕ_1. The thicknesses of four outermost layers of every case are listed as followed, for 40º, **(G)**: 263nm, 161 nm, 294 nm, 92 nm; **(H)**: 263nm, 112nm, 265nm, 112nm; **(I)**: 260nm, 160nm, 224nm, 106nm; for 75º, **(J)**: 262nm, 184 nm, 280 nm, 77 nm; **(K)**: 259nm, 168 nm, 240 nm, 95 nm; **(L)**: 263nm, 124 nm, 269 nm, 99 nm; There are a lot of multilayers that can realize perfect anomalous reflection. The multilayers in (H) and (L) are fabricated in main text.

Table S1. The parameters of two samples in main text (unit: nm).

Thickness of Bragg mirror ((HL)^{7}H)															
Si	SiO_2	Si	SiO_2	Si	SiO_2	Si	SiO_2	Si	SiO_2	Si	SiO_2	Si	SiO_2	Si
109	263	109	263	109	263	109	263	109	263	109	263	109	263	109
			D	C	B	A	d_s	H	x_1	x_2	x_3	x_4	x_5	x_6
Materials			SiO_2	Si	SiO_2	Si	SiO_2	Si	Si	Si	Si	Si	Si	Si
40º sample			263	112	265	112	280	500	71	161	201	217	236	356
75º sample			263	124	269	99	372	315	174	64	264	370	N/A	N/A

5. *75º perfect anomalous reflection*

When the anomalous reflection angle is enlarged from 40° to 75°, the requirement of nonlocality becomes higher as shown in Equation S4 and Fig. S5A. In addition, as shown in Fig. S5B and mentioned in reference (*32*), as the anomalous reflection angle becomes large, the phase deviates from the linear gradient. Hence, using gradient grating is not the best choice to realize perfect anomalous reflection with a large bending angle. Fig. S5C shows the anomalous reflection efficiency versus phase responses while four Si gradient gratings whose width from small to large were selected. The efficiency can be improved significantly by changing the phase response ϕ_0 and ϕ_1 of propagating waves, but the highest efficiency is about 93%. To achieve perfect anomalous reflection, the width of a unit grating is also selected as a parameter for scanning. Fig. S5D shows the result when the first grating and phase responses are scanning parameters. Fig. S5E shows the result when the second grating and phase responses are scanning parameters. Fig. S5F shows the result when the third grating and phase responses are scanning parameters. Fig. S5G shows the result when the fourth grating and phase responses are scanning parameters. All the results indicate that the anomalous reflection efficiency can be controlled in a wide range at will and reach a 99% efficiency.

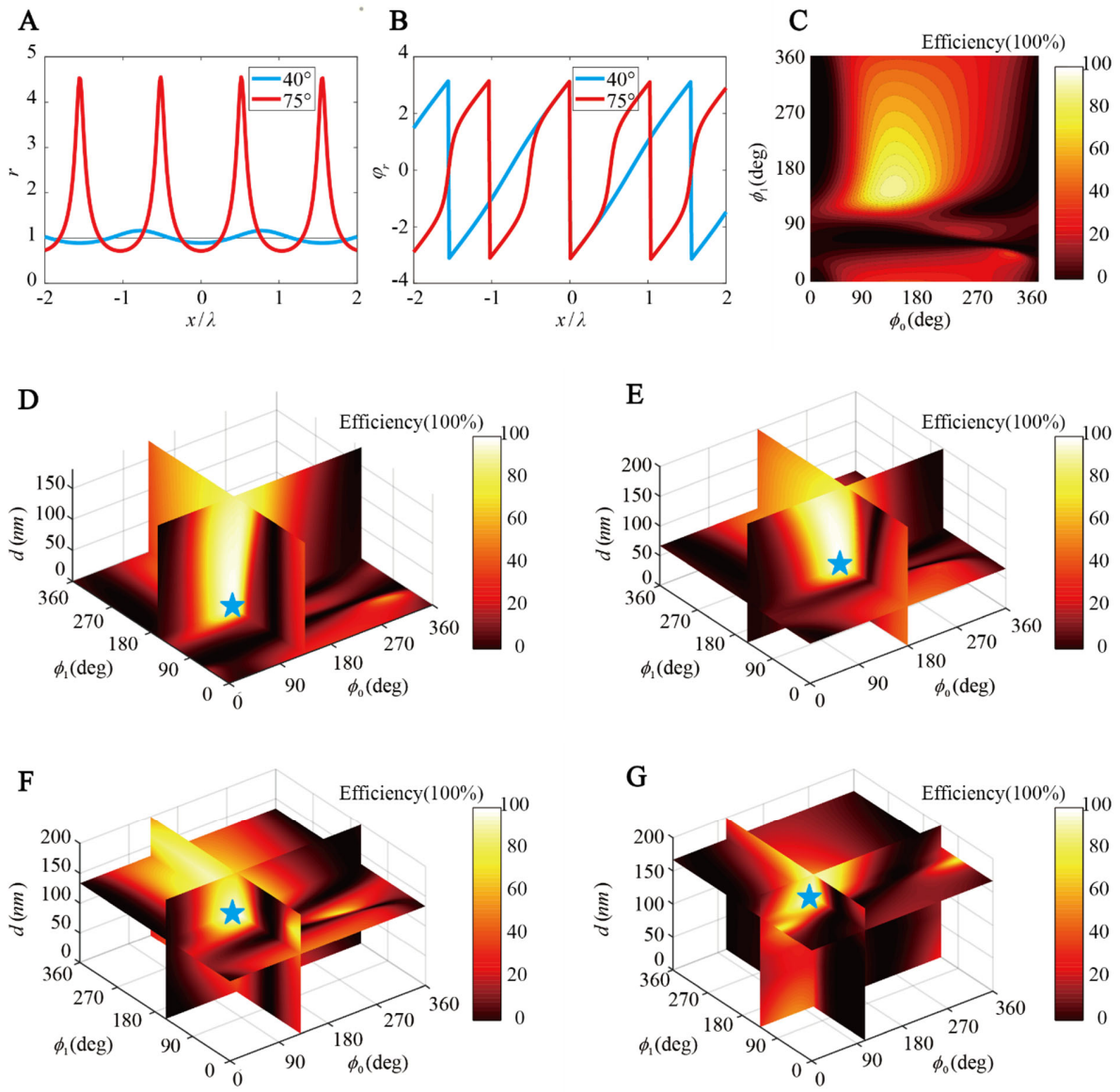

Fig. S5. Analysis of 75º perfect anomalous reflection. (A) The amplitudes $r(x)$ and **(B)** reflection phases $\varphi_r(x)$ for perfect anomalous reflection at small and big angle. **(C)** The anomalous reflection efficiency versus phase responses while four Si gradient gratings whose width from small to large were selected. The scanning results when **(D)** First **(E)** Second **(F)** Third and **(G)** Fourth grating are scanning parameters. The perfect anomalous reflection is marked by blue pentagram.

6. *The complicated functionality realized by Q3D-SWSs*

Using our methodology and structure, it is possible to realize more complicated energy-flow distribution and functionality. Fig. S6 shows the structure of two-dimensional metasurfaces. We demonstrate a polarization-independent perfect anomalous reflection and a polarization-dependent mirror in main text. The detailed parameters are shown in Table S2. On the one hand, the rectangular metasurface is polarization-dependent and has completely different scattering coefficients for TE and TM polarization. On the other hand, the multilayer films are polarization-independent under normal incidence and polarization-dependent under oblique incidence. Therefore, the multilayer films offer a same ϕ_0 and a different ϕ_1 for TE and TM polarization as shown in Fig. S6. By optimizing the combination of polarization-dependent response, the polarization-independent and polarization-dependent mirrors can be obtained. If some approach is adopted to break the polarization insensitivity of ϕ_0, then the polarization properties of Q3D-SWSs will be further developed.

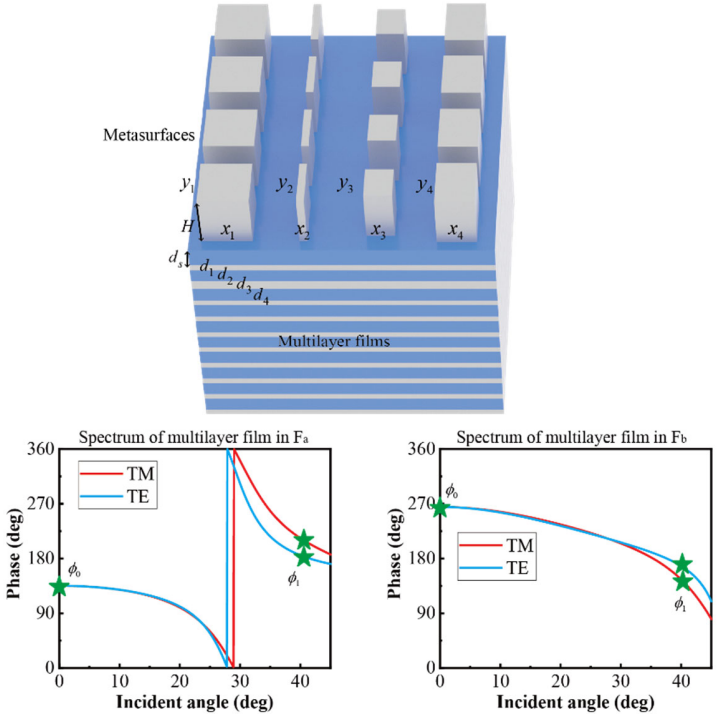

Fig. S6. The schematic diagram and spectra of multilayer films in the two-dimensional metasurfaces.

Table S2. The parameters of metasurfaces (unit: nm) for polarization-independent perfect anomalous reflection (F_a) and polarization-dependent mirror (F_b).

	H	x_1	x_2	x_3	x_4	y_1	y_2	y_3	y_4	d_s	d_1	d_2	d_3	d_4
F_a	499	272	40	149	218	271	271	271	271	801	239	475	484	263
F_b	625	282	106	319	281	239	285	285	285	541	525	207	195	263

7. ***The comparison of our work and published articles***

Fig. S7 shows the comparisons of our work and published work (*24*, *30*, *37*, *45-47*) at optical frequency. The theoretical limit is corresponding to the local design philosophy, i.e. generalized Snell's law. No matter for small or big angle anomalous reflection, we have obtained the highest anomalous reflection efficiency both in design and experiment, demonstrating the validity of our proposed design methodology and structure.

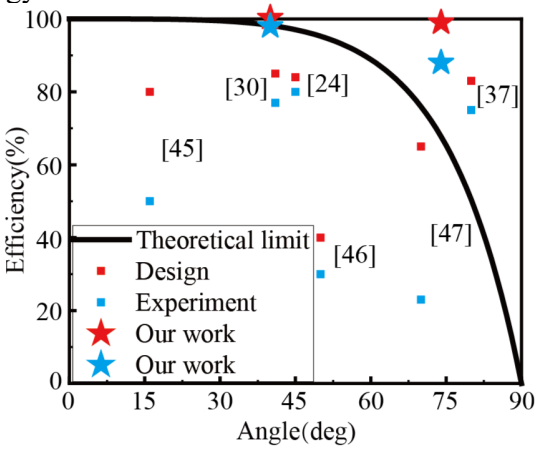

Fig. S7. The comparisons of our work and published work.

8. ***The details about experimental measurement***

To obtain the absolute efficiencies of the anomalous-reflection samples, the incident light has to be characterized first. Therefore, we measure the reflection spectra of two high-reflection mirrors in the 40°- and 75° anomalous-reflection samples by Cary 5000 from Agilent as shown in Fig. S8A. This is a standard test (*48*, *49*) and the obtained results fit well with the calculated spectra. In the measurements by Cary 5000, the monochromatic light is evenly divided into two light paths before it hits the sample surface. One is the test light path, and the other is the reference light path. The sample is put into the test light path and an Al-mirror is put into the reference light path during measurements. The detector receives the test light and reference light at the same time, so as to obtain the spectral information of the sample. Later, angle-resolved spectrum system in micro-region (ARM) from Ideaoptics Inc. as shown in Fig. S8B is employed to verify the spectral property of the 40° anomalous reflection sample. It's worth noting that the high-reflection mirror was tested first to normalize the incident light. The ARM system possess a 180 μm beam spot size which can be further zoomed out. Hence, a 40° anomalous reflection sample with an area of 600 μm square was fabricated to carry out the measurement. The ARM system realizes angle resolution by focusing the reflective beam in the Fourier plane of the lens. The reflective beam spots at different positions in the focal plane represent different reflection angles. Therefore, the maximum reflection angle that the system can test is limited by the numerical aperture of the lens. The 75° anomalous reflection sample was not measurable using the ARM system because it equipped with a microscope objective whose numerical aperture is 0.87 only guarantees a collection angle of 60°. So, the angle-resolved spectrum system in macro-region (R1) from Ideaoptics China is employed to characterize the 75° anomalous reflection sample. This is a device with a spot size of 1 mm, that realizes angle resolution by mechanical rotating of the receiver. In the actual test, the high reflector mirror was used to normalize the incident light and then a 75° anomalous reflection sample with an area of 2 mm square was fabricated to carry out the measurement.

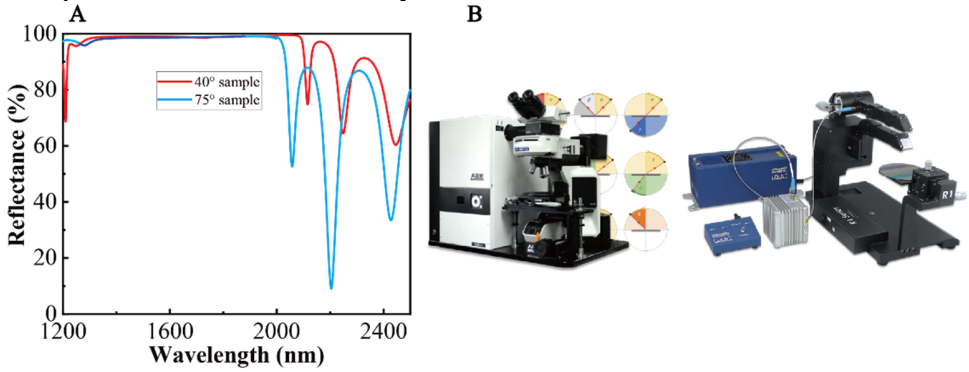

Fig. S8. The experimental spectra and configuration. (A) The experimental spectra of 40º- and 75º-high reflector mirror. **(B)** The angle-resolved spectrum system in micro-region (ARM) and the angle-resolved spectrum system in macro-region (R1) from Ideaoptics Inc.

REFERENCES AND NOTES

1. A. V. Kildishev, A. Boltasseva, V. M. Shalaev, Planar photonics with metasurfaces. *Science* **339**, 1232009 (2013).

2. P. Genevet, F. Capasso, F. Aieta, M. Khorasaninejad, R. Devlin, Recent advances in planar optics: From plasmonic to dielectric metasurfaces. *Optica* **4**, 139–152 (2017).

3. X. Luo, Subwavelength artificial structures: Opening a new era for engineering optics. *Adv. Mater.* **31**, 1804680 (2018).

4. L. Deng, J. Deng, Z. Guan, J. Tao, Y. Chen, Y. Yang, D. Zhang, J. Tang, Z. Li, Z. Li, S. Yu, G. Zheng, H. Xu, C. W. Qiu, S. Zhang, Malus-metasurface-assisted polarization multiplexing. *Light Sci. Appl.* **9**, 101 (2020).

5. W. T. Chen, A. Y. Zhu, F. Capasso, Flat optics with dispersion-engineered metasurfaces. *Nat. Rev. Mater.* **5**, 604–620 (2020).

6. M. Khorasaninejad, K. B. Crozier, Silicon nanofin grating as a miniature chirality-distinguishing beam-splitter. *Nat. Commun.* **5**, 5386 (2014).

7. F. Qin, L. Ding, L. Zhang, F. Monticone, C. C. Chum, J. Deng, S. T. Mei, Y. Li, J. H. Teng, M. H. Hong, S. Zhang, A. Alu, C. W. Qiu, Hybrid bilayer plasmonic metasurface efficiently manipulates visible light. *Sci. Adv.* **2**, e1501168 (2016).

8. A. Arbabi, E. Arbabi, Y. Horie, S. M. Kamali, A. Faraon, Planar metasurface retroreflector. *Nat. Photonics* **11**, 415–420 (2017).

9. M. Faraji-Dana, E. Arbabi, A. Arbabi, S. M. Kamali, H. Kwon, A. Faraon, Compact folded metasurface spectrometer. *Nat. Commun.* **9**, 4196 (2018).

10. S. Wang, P. C. Wu, V. C. Su, Y. C. Lai, M. K. Chen, H. Y. Kuo, B. H. Chen, Y. H. Chen, T. T. Huang, J. H. Wang, R. M. Lin, C. H. Kuan, T. Li, Z. Wang, S. Zhu, D. P. Tsai, A broadband achromatic metalens in the visible. *Nat. Nanotechnol.* **13**, 227–232 (2018).

11. S. Shrestha, A. C. Overvig, M. Lu, A. Stein, N. Yu, Broadband achromatic dielectric metalenses. *Light Sci. Appl.* **7**, 85 (2018).

12. A. Arbabi, E. Arbabi, S. M. Kamali, Y. Horie, S. Han, A. Faraon, Miniature optical planar camera based on a wide-angle metasurface doublet corrected for monochromatic aberrations. *Nat. Commun.* **7**, 13682 (2016).

13. M. Khorasaninejad, W. T. Chen, R. C. Devlin, J. Oh, A. Y. Zhu, F. Capasso, Metalenses at visible wavelengths: Diffraction-limited focusing and subwavelength resolution imaging. *Science* **352**, 1190–1194 (2016).

14. G. Zheng, H. Muhlenbernd, M. Kenney, G. Li, T. Zentgraf, S. Zhang, Metasurface holograms reaching 80% efficiency. *Nat. Nanotechnol.* **10**, 308–312 (2015).

15. L. Jin, Z. Dong, S. Mei, Y. F. Yu, Z. Wei, Z. Pan, S. D. Rezaei, X. Li, A. I. Kuznetsov, Y. S. Kivshar, J. K. W. Yang, C. W. Qiu, Noninterleaved metasurface for (26-1) spin- and wavelength-encoded holograms. *Nano Lett.* **18**, 8016–8024 (2018).

16. S. Liu, P. P. Vabishchevich, A. Vaskin, J. L. Reno, G. A. Keeler, M. B. Sinclair, I. Staude, I. Brener, An all-dielectric metasurface as a broadband optical frequency mixer. *Nat. Commun.* **9**, 2507 (2018).

17. X. Dun, H. Ikoma, G. Wetzstein, Z. Wang, X. Cheng, Y. Peng, Learned rotationally symmetric diffractive achromat for full-spectrum computational imaging. *Optica* **7**, 913–922 (2020).

18. F. Yesilkoy, E. R. Arvelo, Y. Jahani, M. Liu, A. Tittl, V. Cevher, Y. Kivshar, H. Altug, Ultrasensitive hyperspectral imaging and biodetection enabled by dielectric metasurfaces. *Nat. Photonics* **13**, 390–396 (2019).

19. L. Li, Z. Liu, X. Ren, S. Wang, V.-C. Su, M.-K. Chen, C. H. Chu, H. Y. Kuo, B. Liu, W. Zang, G. Guo, L. Zhang, Z. Wang, S. Zhu, D. P. Tsai, Metalens-array–based high-dimensional and multiphoton quantum source. *Science* **368**, 1487–1490 (2020).

20. Z. Wang, T. Li, A. Soman, D. Mao, T. Kananen, T. Gu, On-chip wavefront shaping with dielectric metasurface. *Nat. Commun.* **10**, 3547 (2019).

21. J. Park, B. G. Jeong, S. I. Kim, D. Lee, J. Kim, C. Shin, C. B. Lee, T. Otsuka, J. Kyoung, S. Kim, K. Y. Yang, Y. Y. Park, J. Lee, I. Hwang, J. Jang, S. H. Song, M. L. Brongersma, K. Ha, S. W. Hwang, H. Choo, B. L. Choi, All-solid-state spatial light modulator with independent phase and amplitude control for three-dimensional LiDAR applications. *Nat. Nanotechnol.* **16**, 69–76 (2020).

22. Y. Y. Xie, P. N. Ni, Q. H. Wang, Q. Kan, G. Briere, P. P. Chen, Z. Z. Zhao, A. Delga, H. R. Ren, H. D. Chen, C. Xu, P. Genevet, Metasurface-integrated vertical cavity surface-emitting lasers for programmable directional lasing emissions. *Nat. Nanotechnol.* **15**, 125–130 (2020).

23. P. P. Iyer, R. A. DeCrescent, Y. Mohtashami, G. Lheureux, N. A. Butakov, A. Alhassan, C. Weisbuch, S. Nakamura, S. P. DenBaars, J. A. Schuller, Unidirectional luminescence from InGaN/GaN quantum-well metasurfaces. *Nat. Photonics* **14**, 543–548 (2020).

24. S. Sun, K. Y. Yang, C. M. Wang, T. K. Juan, W. T. Chen, C. Y. Liao, Q. He, S. Xiao, W. T. Kung, G. Y. Guo, L. Zhou, D. P. Tsai, High-efficiency broadband anomalous reflection by gradient meta-surfaces. *Nano Lett.* **12**, 6223–6229 (2012).

25. Z. Li, M.-H. Kim, C. Wang, Z. Han, S. Shrestha, A. C. Overvig, M. Lu, A. Stein, A. M. Agarwal, M. Loncar, N. Yu, Controlling propagation and coupling of waveguide modes using phase-gradient metasurfaces. *Nat. Nanotechnol.* **12**, 675–683 (2017).

26. D. Sell, J. Yang, S. Doshay, R. Yang, J. A. Fan, Large-angle, multifunctional metagratings based on freeform multimode geometries. *Nano Lett.* **17**, 3752–3757 (2017).

27. Q. Huang, Q. Jia, J. Feng, H. Huang, X. Yang, J. Grenzer, K. Huang, S. Zhang, J. Lin, H. Zhou, T. You, W. Yu, S. Facsko, P. Jonnard, M. Wu, A. Giglia, Z. Zhang, Z. Liu, Z. Wang, X. Wang, X. Ou, Realization of wafer-scale nanogratings with sub-50 nm period through vacancy epitaxy. *Nat. Commun.* **10**, 2437 (2019).

28. N. Yu, P. Genevet, M. A. Kats, F. Aieta, J.-P. Tetienne, F. Capasso, Z. Gaburro, Light propagation with phase discontinuities: Generalized laws of reflection and refraction. *Science* **334**, 333–337 (2011).

29. S. Sun, Q. He, S. Xiao, Q. Xu, X. Li, L. Zhou, Gradient-index meta-surfaces as a bridge linking propagating waves and surface waves. *Nat. Mater.* **11**, 426–431 (2012).

30. Z. Y. Li, E. Palacios, S. Butun, K. Aydin, Visible-frequency metasurfaces for broadband anomalous reflection and high-efficiency spectrum splitting. *Nano Lett.* **15**, 1615–1621 (2015).

31. C. Pfeiffer, A. Grbic, Metamaterial Huygens' surfaces: Tailoring wave fronts with reflectionless sheets. *Phys. Rev. Lett.* **110**, 197401 (2013).

32. N. M. Estakhri, A. Alu, Wave-front transformation with gradient metasurfaces. *Phys. Rev. X* **6**, 041008 (2016).

33. A. Epstein, G. V. Eleftheriades, Synthesis of passive lossless metasurfaces using auxiliary fields for reflectionless beam splitting and perfect reflection. *Phys. Rev. Lett.* **117**, 256103 (2016).

34. D. H. Kwon, S. A. Tretyakov, Perfect reflection control for impenetrable surfaces using surface waves of orthogonal polarization. *Phys. Rev. B* **96**, 085438 (2017).

35. A. Epstein, G. V. Eleftheriades, Shielded Perfect Reflectors Based on Omega-Bianisotropic Metasurfaces, in *Proceedings of the 2017 International Workshop on Antenna Technology: Small Antennas, Innovative Structures, and Applications* (*iWAT*) (IEEE, 2017).

36. A. Díaz-Rubio, V. S. Asadchy, A. Elsakka, S. A. Tretyakov, From the generalized reflection law to the realization of perfect anomalous reflectors. *Sci. Adv.* **3**, e1602714 (2017).

37. V. S. Asadchy, A. Wickberg, A. Diaz-Rubio, M. Wegener, Eliminating scattering loss in anomalously reflecting optical metasurfaces. *ACS Photonics* **4**, 1264–1270 (2017).

38. D. Fattal, J. Li, Z. Peng, M. Fiorentino, R. G. Beausoleil, Flat dielectric grating reflectors with focusing abilities. *Nat. Photonics* **4**, 466–470 (2010).

39. S. J. Byrnes, A. Lenef, F. Aieta, F. Capasso, Designing large, high-efficiency, high-numerical-aperture, transmissive meta-lenses for visible light. *Opt. Express* **24**, 5110–5124 (2016).

40. M. Kang, Y. Ra'di, D. Farfan, A. Alù, Efficient focusing with large numerical aperture using a hybrid metalens. *Phys. Rev. Appl.* **13**, 044016 (2020).

41. Ideaoptics Company Page (2021); www.ideaoptics.com/ [accessed 10 June 2021).

42. P. Lalanne, G. M. Morris, Highly improved convergence of the coupled-wave method for TM polarization. *J. Opt. Soc. Am. A* **13**, 779–784 (1996).

43. K. Ito, H. Iizuka, Highly efficient -1st-order reflection in Littrow mounted dielectric double-groove grating. *AIP Adv.* **3**, 062119 (2013).

44. T. Matsui, A. Miura, N. Ikeda, H. Fujikawa, Y. Sugimoto, N. Engheta, H. Iizuka, Experimental investigation of double-groove grating satisfying total internal reflection condition. *Opt. Express* **22**, 25362–25370 (2014).

45. A. Pors, O. Albrektsen, I. P. Radko, S. I. Bozhevolnyi, Gap plasmon-based metasurfaces for total control of reflected light. *Sci. Rep.* **3**, 2155 (2013).

46. S. Gao, W. Yue, C.-S. Park, S.-S. Lee, E.-S. Kim, D.-Y. Choi, Aluminum plasmonic metasurface enabling a wavelength-insensitive phase gradient for linearly polarized visible light. *ACS Photonics* **4**, 322–328 (2017).

47. S. Gao, S. S. Lee, E. S. Kim, D. Y. Choi, Vertically integrated visible and near-infrared metasurfaces enabling an ultra-broadband and highly angle-resolved anomalous reflection. *Nanoscale* **10**, 12453–12460 (2018).

48. X. Cheng, J. Zhang, T. Ding, Z. Wei, H. Li, Z. Wang, The effect of an electric field on the thermomechanical damage of nodular defects in dielectric multilayer coatings irradiated by nanosecond laser pulses. *Light Sci. Appl.* **2**, e80 (2013).

49. X. Cheng, S. Dong, S. Zhi, S. Paschel, I. Balasa, D. Ristau, Z. Wang, Waterproof coatings for high-power laser cavities. *Light Sci. Appl.* **8**, 12 (2019).